processes

MDPI

Article

A Mechanistic Model Based on Statistics for the Prediction of a Converter's End-Point Molten Steel Temperature

Fang Gao [1], Dazhi Wang [1], Yanping Bao [1,*], Xin Liu [1], Lidong Xing [1,2] and Lihua Zhao [3,*]

[1] State Key Laboratory of Advanced Metallurgy, University of Science and Technology Beijing, Beijing 100083, China; d202110626@xs.ustb.edu.cn (F.G.); b20180528@sx.ustb.edu.cn (D.W.); l15755584029@163.com (X.L.); xinglidong@ustb.edu.cn (L.X.)
[2] Technical Support Center for Prevention and Control of Disastrous Accidents in Metal Smelting, University of Science and Technology Beijing, Beijing 100083, China
[3] School of Metallurgical and Ecological Engineering, University of Science and Technology Beijing, Beijing 100083, China
* Correspondence: baoyp@ustb.edu.cn (Y.B.); zhaolihua@metall.ustb.edu.cn (L.Z.)

Abstract: With the high efficiency and automation of converter smelting, it is becoming increasingly important to predict and control the endpoint temperature of the converter. Based on the heat balance, a model for predicting the molten pool temperature in a converter was established. Moreover, the statistical method of multiple linear regression was used to calculate the converter heat loss coefficient, greatly improving the prediction accuracy of the mechanistic model. Using the model, the oxidation process for each element in the molten pool, the melting processes of scrap, and the flux were also calculated. The model could better approximate the actual smelting process. Data from a 130 t converter were collected to validate the model. When the error ranges were limited to ±20 and ±15 °C, the model hit rates were 96 and 86.7%, respectively.

Keywords: converter; endpoint temperature; model; heat loss coefficient; multiple linear regression

Citation: Gao, F.; Wang, D.; Bao, Y.; Liu, X.; Xing, L.; Zhao, L. A Mechanistic Model Based on Statistics for the Prediction of a Converter's End-Point Molten Steel Temperature. *Processes* **2023**, *11*, 2233. https://doi.org/10.3390/pr11082233

Academic Editor: Miguel Ladero Galán

Received: 18 June 2023
Revised: 17 July 2023
Accepted: 20 July 2023
Published: 25 July 2023

1. Introduction

The steel industry is the backbone of the manufacturing industry, and provides a widely applicable basic raw material [1–3]. Generally, the steel production process includes iron making, steel making, refining, continuous casting, and hot rolling or cold rolling. The production of converter steel accounts for more than 80% of the total steel production [4]. Converter steelmaking is essential for the entire steel production process. During the smelting process, maintaining reasonable control over the endpoint temperature of the converter plays a pivotal role in the steel quality, product cost, and production operation [5–7]. Most small- and medium-sized steel enterprises in China adopt the empirical steelmaking method [8]. This method is mainly dependent on the technical skill of the production staff, with low control accuracy. In recent years, the application of technologies such as sublances and flue gas analysis equipment has somewhat improved the accuracy of the endpoint control of converters [9,10]. However, the installation of sublance or flue gas analysis equipment on small- and medium-sized converters is challenging. The development of models designed for the quality prediction of the converter steelmaking process to ensure safe production and improve product performance has attracted increasing attention from researchers [11,12].

The development of an accurate prediction model is challenging due to the high-temperature black box process of the converter production. Currently, the widely used converter modeling methods can be roughly divided into two categories: mechanistic models and data-driven models [13–16]. Data-driven models are built by mining the potential relationships between data. Many common data analysis methods have been used to build converter prediction models, such as the support vector machine [17], the

least-squares support-vector machine [18], the extreme learning machine [19], and neural networks [20]. The complexity and variability of the converter production process result in a data-driven model that must be frequently updated to ensure that its accuracy meets the requirements. The data-driven model requires a large amount of complete and accurate data, which is undoubtedly difficult for most steel enterprises to achieve. Mechanistic models are based on the chemical reactions, energy balance, and mass balance in the converter [21–24]. When developing a mechanistic model, some assumed parameters or empirical parameters are usually used, meaning that the model reflects the differences between the different heat data with difficulty. The prediction accuracy of mechanistic models is low due to the heterogeneity of each heat data.

To solve the problem of the relatively low accuracy of traditional mechanistic models, a converter temperature prediction model was developed in this study by combining a mechanistic model and data statistics. This model is based on the basic reaction principle, material and heat balances. The traditional method of calculating the fixed heat loss coefficient has been changed. With this model, the heat loss coefficient is calculated via multiple linear regression to better reflect the variability between heat data. The elemental reactions of the molten steel, scrap, and flux-melting processes during the converter-blowing process are also considered in this model. This method effectively improves the prediction accuracy of the model.

2. The Establishment of a Converter Temperature Prediction Model

2.1. The Heat Balance of a Converter

In this study, the converter temperature prediction model is based on the heat balance of the converter. Figure 1 shows the heat balance of the converter. Generally, the converter heat income includes the physical heat of the hot metal, the oxidation heat of the elements, and the dust oxidation heat; the dust oxidation heat can also be attributed to the oxidation of the iron element. The heat expenditure of the converter includes the physical heat of the molten steel, the physical heat of the slag, the physical heat of the dust, the physical heat of the furnace gas, the physical heat of the sputtering metal, the physical heat of the iron beads in the slag, and the heat loss.

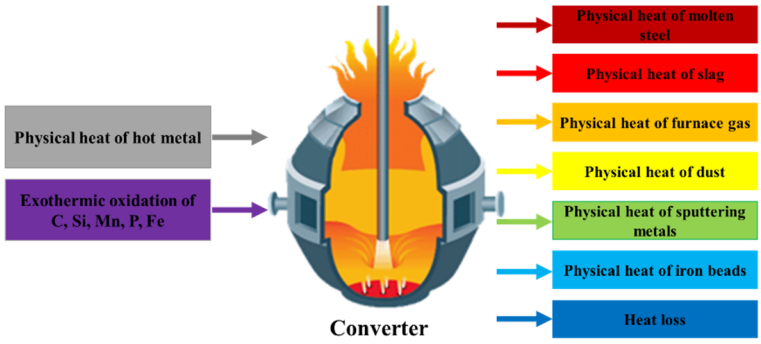

Figure 1. The heat balance of the converter.

The method used to calculate the physical heat of the hot metal is shown in Equation (1). The melting point of the hot metal is calculated as shown in Equation (2).

$$Q_{\text{Hot metal}} = W_{\text{Hot metal}} \times \left[c_m^s \times \left(T_{\text{Hot metal}}^{mp} - 25 \right) + q_m + c_m^l \times \left(T_{\text{Hot metal}} - T_{\text{Hot metal}}^{mp} \right) \right] \quad (1)$$

$$T_{\text{Hot metal}}^{mp} = 1539 - (100 \times w_{HC} + 8 \times w_{HSi} + 5 \times w_{HMn} + 30 \times w_{HP} + 25 \times w_{HS}) - 4 \quad (2)$$

where $Q_{\text{Hot metal}}$ is the physical heat of the hot metal, kJ; $W_{\text{Hot metal}}$ is the amount of hot metal, kg; c_m^s and c_m^l are the solid-specific heat capacity and liquid-specific heat capacity of pig iron, respectively, kJ/(kg·°C); $T_{\text{metal}}^{\text{mp Hot}}$ is the melting point of the hot metal, °C; $T_{\text{Hot metal}}$ is the temperature of the hot metal, °C; q_m is the latent heat of melting the pig iron, kJ/kg;

and w_{HC}, w_{HSi}, w_{HMn}, w_{HP} and w_{HS} are the contents of carbon (C), silicon (Si), manganese (Mn), phosphorus (P) and sulfur (S) in the hot metal, respectively, wt%.

The heat of the oxidation of the elements in the melt pool can be described using Equations (3)–(9).

$$Q_C = (109,500 \times x_{co} + 345,200 \times x_{co_2}) \times (W_{\text{Hot metal}} \times (w_{HC} - w_{MC}) + W_{MScrap} \times (w_{SC} - w_{MC})) \quad (3)$$

$$Q_{Si} = 283,140 \times (W_{\text{Hot metal}} \times (w_{HSi} - w_{MSi}) + W_{MScrap} \times (w_{SSi} - w_{MSi})) \quad (4)$$

$$Q_{Mn} = 70,200 \times (W_{\text{Hot metal}} \times (w_{HMn} - w_{MMn}) + W_{MScrap} \times (w_{SMn} - w_{MMn})) \quad (5)$$

$$Q_P = 189,230 \times (W_{\text{Hot metal}} \times (w_{HP} - w_{MP}) + W_{MScrap} \times (w_{SP} - w_{MP})) \quad (6)$$

$$Q_{Fe} = 5020 \times \frac{56}{72} \times W_{FeO} + 6670 \times \frac{112}{160} \times W_{Fe_2O_3} \quad (7)$$

$$Q_{SiO_2} = 20,700 \times \frac{60}{28} \times (W_{\text{Hot metal}} \times (w_{HSi} - w_{MSi}) + W_{MScrap} \times (w_{SSi} - w_{MSi})) \quad (8)$$

$$Q_{P_2O_5} = 50,200 \times \frac{142}{62} \times (W_{\text{Hot metal}} \times (w_{HP} - w_{MP}) + W_{MScrap} \times (w_{SP} - w_{MP})) \quad (9)$$

where Q_C, Q_{Si}, Q_{Mn}, Q_P, and Q_{Fe} are the exothermic oxidation of carbon, silicon, manganese, phosphorus, and iron, respectively, kJ; Q_{SiO_2} and $Q_{P_2O_5}$ are the slagging heat of SiO_2 and P_2O_5, respectively, kJ; x_{CO} and x_{CO_2} are the ratios of the carbon oxidation reaction needed to produce CO and CO_2, respectively; w_{SC}, w_{SSi}, w_{SMn}, and w_{SP} are the contents of C, Si, Mn, and P in scrap, respectively, wt%; w_{MC}, w_{MSi}, w_{MMn}, and w_{MP} are the contents of C, Si, Mn, and P in molten steel in the melt pool, wt%; W_{FeO} and $W_{Fe_2O_3}$ are the concentrations of FeO and Fe_2O_3 in slag and dust, respectively, kg; and W_{MScrap} is the weight of melted scrap, kg.

The heat income is the sum of the heat of the oxidation of the elements and the physical heat of the hot metal, as shown in Equation (10).

$$Q_{Income} = Q_{\text{Hot metal}} + Q_C + Q_{Si} + Q_{Mn} + Q_P + Q_{Fe} + Q_{SiO2} + Q_{P_2O_5} \quad (10)$$

The method used to calculate the physical heat of the molten steel is expressed in Equation (11), and the melting point of molten steel is calculated using Equation (12).

$$Q_{\text{Molten steel}} = W_M \times \left[c_s^s \times \left(T^{mp}_{\text{Molten steel}} - 25 \right) + q_s + c_s^l \times \left(T_M - T^{mp}_{\text{Molten steel}} \right) \right] \quad (11)$$

$$T^{mp}_{\text{Molten steel}} = 1539 - (65 \times w_{TC} + 8 \times w_{TSi} + 5 \times w_{TMn} + 30 \times w_{TP} + 25 \times w_{TS}) - 4 \quad (12)$$

where $Q_{\text{Molten steel}}$ is the physical heat of the molten steel, kJ; W_M is the amount of molten steel in the melt pool, kg; c_s^s and c_s^l are the solid-specific heat capacity and liquid-specific heat capacity of steel, respectively, kJ/(kg·°C); $T^{mp}_{\text{Molten steel}}$ is the melting point of molten steel, °C; T_M is the temperature of the molten steel in the melt pool, °C; q_s is the latent heat of the melting of steel, kJ/kg; and w_{TC}, w_{TSi}, w_{TMn}, w_{TP}, and w_{TS} are the contents of C, Si, Mn, P and S in molten steel, respectively, wt%.

Equation (13) describes the calculation for the physical heat of steel slag.

$$Q_{Slag} = W_{Slag} \times \left[c_{Slag} \times (T_M - 25) + q_{Slag} \right] \quad (13)$$

The physical heat of dust can be described using Equation (14).

$$Q_{Dust} = W_{Dust} \times \left[c_{Dust} \times (1450 - 25) + q_{Dust} \right] \quad (14)$$

The physical heat of furnace gas can be described using Equation (15).

$$Q_{Gas} = W_{Gas} \times c_{Gas} \times (1450 - 25) \tag{15}$$

The physical heat of iron beads in slag can be described using Equation (16).

$$Q_{Iron\ bead} = W_{Iron\ bead} \times \left[c_m^s \times \left(T_{Molten\ steel}^{mp} - 25\right) + q_m + c_m^l \times \left(T_M - T_{Molten\ steel}^{mp}\right)\right] \tag{16}$$

The physical heat of sputtering metal can be described using Equation (17).

$$Q_{Splash} = W_{Splash} \times \left[c_m^s \times \left(T_{Molten\ steel}^{mp} - 25\right) + q_m + c_m^l \times \left(T_{Molten\ steel} - T_{Molten\ steel}^{mp}\right)\right] \tag{17}$$

where Q_{Slag}, Q_{Dust}, Q_{Gas}, $Q_{Iron\ bead}$, and Q_{Splash} are the physical heat of the steel slag, dust, furnace gas, iron beads in slag, and sputtering metal, respectively, kJ; W_{Slag}, W_{Dust}, W_{Gas}, $W_{Iron\ bead}$, and W_{Splash} are the weight of the steel slag, dust, furnace gas, iron beads in slag, sputtering metal, respectively, kg; c_{Slag}, c_{Dust}, and c_{Gas} are the specific heat capacity of the steel slag, dust, furnace gas, respectively, kJ/(kg·°C); and q_{Slag} and q_{Dust} are the latent heat of the melting of the steel slag and dust, respectively, kJ/kg.

The heat loss of the converter can be calculated using Equation (18).

$$Q_{Loss} = \gamma_{Loss} \times Q_{Income} \tag{18}$$

where Q_{Loss} is the heat loss of the converter, kJ; and γ_{Loss} is the heat loss coefficient of the converter.

As expressed in Equation (19), the sum of the heat expenditure of the converter is equal to the heat revenue. Therefore, the converter bath temperature can be obtained using Equation (20).

$$Q_{Outcome} = Q_{Molten\ steel} + Q_{Slag} + Q_{Dust} + Q_{Iron\ bead} + Q_{Splash} + Q_{Loss} = Q_{Income} \tag{19}$$

$$T_M = \frac{\begin{array}{c} Q_{Income} - Q_{Gas} - Q_{Dust} - Q_{Iron\ bead} - Q_{Splash} - Q_{Loss} \\ -W_M \times \begin{pmatrix} c_s^s \times \left(T_{Molten\ steel}^{mp} - 25\right) + q_s \\ -c_s^l \times T_M^{mp} \end{pmatrix} \\ -W_{Slag} \times \left(q_{Slag} - c_{Slag} \times 25\right) \end{array}}{W_M \times c_s^l + W_{Slag} \times c_{Slag}} \tag{20}$$

To calculate the molten steel temperature in the melt pool, it is necessary to obtain the following information:

(1) Contents of carbon, silicon, manganese, and phosphorus in the molten steel in the melt pool;
(2) Quantity of steel slag and molten steel;
(3) Heat loss coefficient.

2.2. Calculation Model of Molten Steel Element Content in Molten Pool

During the converter-smelting process, the chemical elements in the molten pool will react with oxygen. Generally, oxygen mainly reacts with silicon and manganese in the early stage of blowing, and the oxidation reaction rate of carbon gradually increases. In the middle stage of blowing, oxygen mainly reacts with carbon due to the low silicon and manganese contents, and the reaction rate of decarburization reaches the maximum. In the blowing final stage, the reaction rate of decarburization decreases with the decrease in the carbon content of the molten pool. The decarburization reaction in the converter molten pool is shown in Equations (21) and (22).

$$[C] + [O] = CO \tag{21}$$

$$[C] + 2[O] = CO_2 \tag{22}$$

Therefore, the decarburization process is usually attributed to a three-stage process. In the early-blowing process stage, the decarburization rate shows a linear increasing trend with time. In the middle-blowing process stage, the decarburization rate is constant, and its magnitude is related to the oxygen flow rate. In the final blowing process stage, the decarburization rate linearly decreases with the decreasing carbon content (Figure 2). The decarburization rates of the three stages of the converter-blowing process are shown in Equations (23)–(25), respectively [23].

$$-\frac{dC}{dt} = W_M \beta \frac{h_{min}}{h} \frac{Q_{top}}{Q_{topmax}} k_1 t \tag{23}$$

$$-\frac{dC}{dt} = W_M \beta \frac{h_{min}}{h} \frac{Q_{top}}{Q_{topmax}} \alpha v_{Oxygen} \tag{24}$$

$$-\frac{dC}{dt} = W_M \beta \frac{h_{min}}{h} \frac{Q_{top}}{Q_{topmax}} k_3 \left(C_{[C]} - C_0 \right) \tag{25}$$

where β is the constant coefficient; h is the oxygen lance height, m; α is the decarburization oxygen efficiency, wt%/kg; h_{min} is the lowest oxygen lance height, m; Q_{top} is the oxygen flow rate, Nm^3/h; Q_{topmax} is the maximum oxygen flow rate, Nm^3/h; $C_{[C]}$ is the carbon content, wt%; C_0 is the ultimate carbon content, wt%; and k_i (i = 1,3) is the constant coefficient.

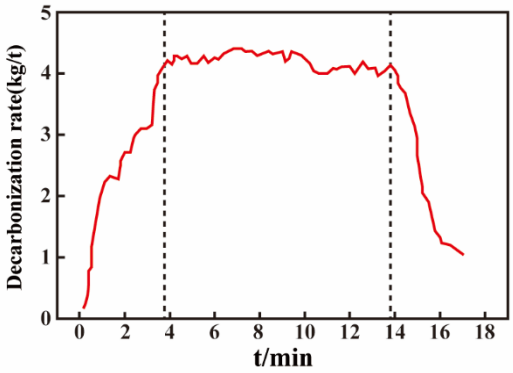

Figure 2. The typical decarbonization rate during the blowing process of the converter.

Silicon, manganese, phosphorus, and iron also oxidized during the blowing process of the converter. Generally, there are two reaction zones in the converter: the oxygen jet reaction zone formed by the high-speed impact of oxygen on the surface of the melt pool and the slag–metal reaction zone formed by the slag and the metal surface (Figure 3).

The oxidation reactions of Si, Mn, and Fe expressed in Equations (26)–(29) occur in the oxygen jet reaction zone. The reaction shown in Equations (30)–(32) occurs in the slag–metal interface reaction zone.

$$[Si] + O_2 = (SiO_2) \tag{26}$$

$$[Mn] + \frac{1}{2}O_2 = (MnO) \tag{27}$$

$$[Fe] + \frac{1}{2}O_2 = (FeO) \tag{28}$$

$$2[Fe] + \frac{3}{2}O_2 = (Fe_2O_3) \tag{29}$$

$$[Si] + 2(FeO) = (SiO_2) + 2[Fe] \tag{30}$$

$$[Mn] + (FeO) = (MnO) + [Fe] \quad (31)$$

$$2[P] + 5(FeO) = 5[Fe] + (P_2O_5) \quad (32)$$

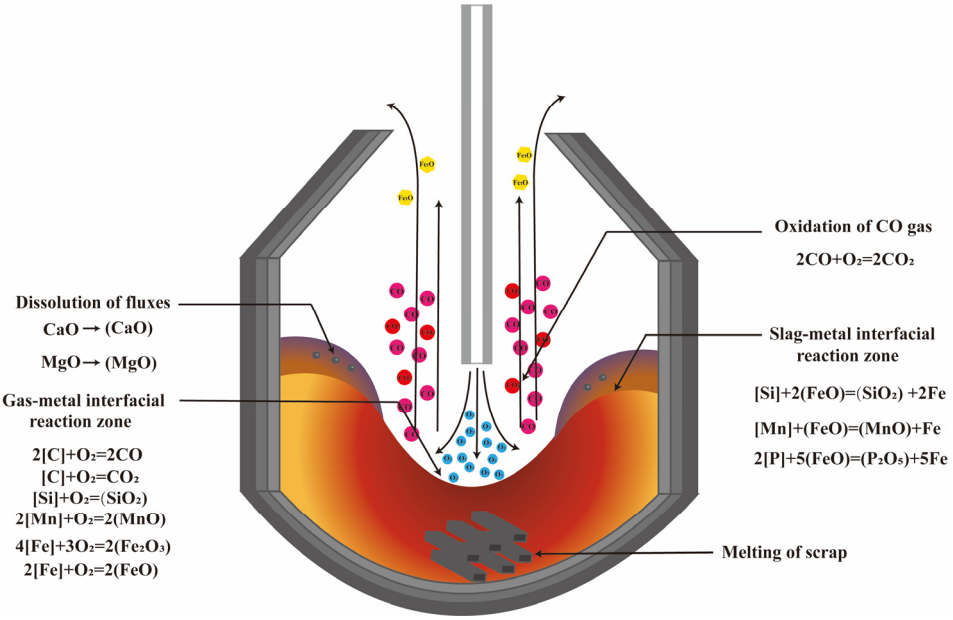

Figure 3. Schematic diagram of a reaction zone in each area of the converter.

In this study, a dual reaction zone model was developed to calculate the oxidation rates of silicon, manganese, and phosphorus.

The desiliconization and demanganization reactions of the converter mainly occur in the oxygen jet reaction zone and slag–metal reaction zone. According to the kinetics of desilication and demanganization in the two reaction zones, the calculation models for the silicon and manganese contents in the molten pool are developed.

The desiliconization and demanganization reaction rates can be expressed as Equations (33) and (34), respectively.

$$-\frac{dSi}{dt} = A_{iz}k_{gm}\rho_m\left(w_{MSi} - [Si\%]_{gm}\right)/100 + A_{sm}k_{sm}\rho_m(w_{MSi} - [Si\%]_{sm})/100 \quad (33)$$

$$-\frac{dMn}{dt} = A_{iz}k_{gm}\rho_m\left(w_{MMn} - [Mn\%]_{gm}\right)/100 + A_{sm}k_{sm}\rho_m(w_{MMn} - [Mn\%]_{sm})/100 \quad (34)$$

The dephosphorization reaction mainly occurs in the slag–metal reaction zone. The dephosphorization reaction rate can be expressed as follows:

$$-\frac{dP}{dt} = A_{sm}k_{sm}\rho_m(w_{MP} - [P\%]_{sm})/100 \quad (35)$$

where $-dSi/dt$, $-dMn/dt$, and $-dP/dt$ are the desiliconization reaction rate, the demanganization reaction rate, and the dephosphorization reaction rate, respectively, $kg{\cdot}s^{-1}$; A_{iz} is the interfacial area of gas–metal reaction, m^2; Ref. [23] k_{gm} is the mass transfer coefficient at the gas–metal interface, m/s; Ref. [24] A_{sm} is the interfacial area of slag–metal reaction, m^2; Ref. [23] k_{sm} is the mass transfer coefficient at the slag–metal interface, m/s; Ref. [24] ρ_m is the density of the molten steel, kg/m^3; $[j\%]_{sm}$ is the interface concentration of j at the slag–metal interface, wt%, j = Si, Mn, P; and $[j\%]_{gm}$ is the interface concentration of j at the gas–metal interface, wt%, j = Si and Mn.

The amount of Fe oxide produced is calculated according to the oxygen balance. All oxygen entering the converter bath reacts with Fe to form FeO or Fe_2O_3, except for

the oxygen involved in the oxidation of C, Si, Mn, P, and S, the oxygen dissolved in the steel, and the directly dissipated oxygen. The little oxygen consumed by the secondary combustion of CO is considered in this study. The amount of oxygen consumed by Fe can be calculated using Equation (36)

$$V_{Fe\_O} = \left(V_{O_2}^{In} - V_{O_2}^{Reaction} - V_{O_2}^{Dissolution} - V_{O_2}^{Dissipation}\right) \quad (36)$$

where V_{Fe_O} is the amount of oxygen consumed by Fe, Nm^3; $V_{O_2}^{In}$ is the amount of oxygen entering the converter, Nm^3; $V_{O_2}^{Reaction}$ is the amount of oxygen involved in the oxidation of C, Si, Mn, P, and S, Nm^3; $V_{O_2}^{Dissolution}$ is the amount of oxygen dissolved in the steel, Nm^3; and $V_{O_2}^{Dissipation}$ is the amount of oxygen directly dissipated, Nm^3.

The amount of FeO and Fe_2O_3 generated can be calculated using Equations (37) and (38).

$$W_{FeO} = x_{FeO} \times V_{Fe\_O} \times \frac{32}{22.4} \times \frac{72}{16} \quad (37)$$

$$W_{Fe_2O_3} = (1 - x_{FeO}) \times V_{Fe\_O} \times \frac{32}{22.4} \times \frac{112}{48} \quad (38)$$

where x_{FeO} is the ratio of the Fe oxidation reaction required to produce FeO.

2.3. Calculation of Steel Slag Quantity

In the process of converter smelting, the oxidation products of C, Si, Mn, P, S, and Fe will form steel slag on the surface of molten steel, together with the added fluxes. In addition, the steel slag will absorb some heat during the formation process. Therefore, it is crucial to determine the amount of steel slag in the smelting process. The amount of steel slag is calculated according to the material balance of the molten pool, as expressed in Equation (39).

$$W_{Slag} = W_{Iron-slag} + W_{Retention-slag} + W_{SiO_2} + W_{MnO} + W_{P_2O_5} + W_{CaS} + W_{sFeO} + W_{sFe_2O_3} + W_{Lime} + W_{Mg-ball} + W_{LBD} \quad (39)$$

where W_{Slag} is the weight of slag, kg; $W_{Iron\text{-}slag}$ is the weight of iron slag brought into the converter, kg; W_{SiO_2}, W_{MnO}, $W_{P_2O_5}$, W_{CaS}, W_{sFeO}, and $W_{sFe_2O_3}$ are the weights of the oxidation products entering the slag after the oxidation of Si, Mn, P, S, and Fe in the melt pool, respectively, kg; W_{Lime} is the weight of melted lime, kg; $W_{Mg\text{-}ball}$ is the weight of melted magnesium ball, kg; and W_{LBD} is the weight of melted lightly burned dolomite, kg.

The weights of the oxidation products produced by the oxidation reactions of Si, Mn, P, and S in the bath can be calculated using Equations (40)–(43).

$$W_{SiO_2} = 0.021429 \times W_M \times (w_{HSi} - w_{MSi}) \quad (40)$$

$$W_{MnO} = 0.1224 \times W_M \times (w_{HMn} - w_{MMn}) \quad (41)$$

$$W_{P_2O_5} = 0.229 \times W_M \times (w_{HP} - w_{MP}) \quad (42)$$

$$W_{CaS} = 0.225 \times W_M \times (w_{HS} - w_{MS}) \quad (43)$$

Because of the melting process, after the addition of fluxes to the converter, the slag composition at a certain time cannot be directly calculated according to the amount of fluxes added. However, the slag composition will be calculated based on the amount of flux melted. Many scholars have studied the dissolution behavior of lime in the converter melt pool [25–28]. Figure 4 shows the schematic diagram of the lime-melting process. The process of lime dissolution in the steel slag is as follows:

(1) Due to the infiltration of FeO in the slag to the interior of the lime, the lime gradually dissolves in the slag, thus increasing the CaO content at the interface;

(2) SiO_2 in the slag is enriched on the lime surface and reacts with CaO to form a 2CaO–SiO_2 layer;
(3) FeO continues to diffuse from the slag into the reaction interface;
(4) The liquid-phase layer of CaO–FeO with a high FeO content is formed between the 2CaO–SiO_2 layer and the lime;
(5) The 2CaO–SiO_2 layer peels off and dissolves in the slag under the action of the CaO–FeO liquid-phase layer with a high FeO content.

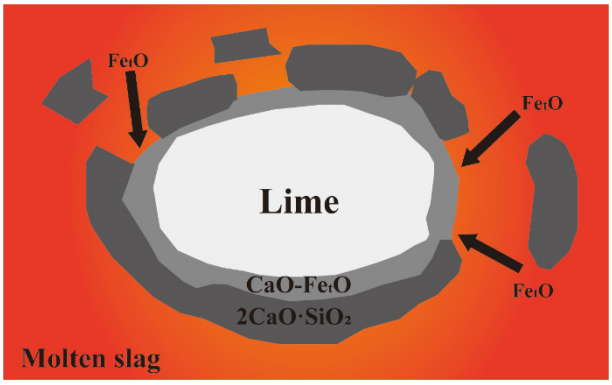

Figure 4. The schematic diagram of the lime-melting process.

The dissolution rate of lime in steel slag mainly depends on the slag temperature and composition. It is assumed that the mass transfer within the boundary layer between the slag and lime is the limiting link. The dissolution rate of lime can be expressed as follows:

$$v_{CaO} = \frac{k\rho_s A_{CaO}}{100}(c_s - c_b) \quad (44)$$

where v_{CaO} is the dissolution rate of lime in slag, g/s; k is the mass transfer coefficient, cm/s; A_{CaO} is the surface area of lime, cm^2; c_s and c_b are the CaO contents in the saturated slag and slag body, respectively, wt.%; and ρ_s is the slag density, g/cm^3.

2.4. Calculation of Molten Steel Quantity in Molten Pool

In the hot metal reaction production of molten steel, the weight loss mainly includes the oxidation of C, Si, Mn, P, S, and Fe. The oxidation amount of C, Si, Mn, P, and S in the bath can be calculated using Equations (45)–(49).

$$\Delta W_{HC} = 0.01 \times \left(W_{Hot\ metal} \times (w_{HC} - w_{MC}) + W_{MScrap} \times (w_{SC} - w_{MC})\right) \quad (45)$$

$$\Delta W_{HSi} = 0.01 \times \left(W_{Hot\ metal} \times (w_{HSi} - w_{MSi}) + W_{MScrap} \times (w_{SSi} - w_{MSi})\right) \quad (46)$$

$$\Delta W_{HMn} = 0.01 \times \left(W_{Hot\ metal} \times (w_{HMn} - w_{MMn}) + W_{MScrap} \times (w_{SMn} - w_{MSi})\right) \quad (47)$$

$$\Delta W_{HP} = 0.01 \times \left(W_{Hot\ metal} \times (w_{HP} - w_{MP}) + W_{MScrap} \times (w_{SP} - w_{MSi})\right) \quad (48)$$

$$\Delta W_{HS} = 0.01 \times \left(W_{Hot\ metal} \times (w_{HS} - w_{MS}) + W_{MScrap} \times (w_{SS} - w_{MS})\right) \quad (49)$$

where ΔW_{HC}, ΔW_{HSi}, ΔW_{HMn}, ΔW_{HP}, ΔW_{HS} are the weight loss of C, Si, Mn, P, and S in the bath, respectively, kg.

The loss of Fe in the molten pool mainly occurs via iron oxide in slag and iron beads in slag and smoke dust. In this study, 8% is assumed to be the quantity of iron beads in slag. The loss of iron in the molten pool is shown in Equation (50).

$$\Delta W_{Fe} = W_{FeO} \times \frac{56}{72} + W_{Fe_2O_3} \times \frac{112}{160} + 0.08 \times W_{Slag} \quad (50)$$

where ΔW_{Fe} is the weight of iron loss in the molten pool, kg.

The weight of molten steel in the bath is related to the weight of molten scrap. The melting mechanism of scrap in molten metal has been studied [29–33]. In the early and middle stages of converter blowing, the liquid-phase line temperature of the scrap is higher than the melt bath temperature, and the scrap-melting process is controlled by the mass transfer process of carbon. In the final stage of converter blowing, the liquidus temperature of scrap is lower than the temperature of the molten pool, and the melting process of scrap is controlled by the heat transfer process. Xu et al. studied the scrap-melting process under different conditions and developed models for calculating the scrap-melting rate under the control of heat and mass transfer processes [34].

Figure 5 shows the temperature and concentration distributions during scrap melting. When the melting rate of scrap depends on the rate of heat transfer from the molten pool to the scrap, the melting rate of scrap can be expressed as follows:

$$V_{Scrap} = -\frac{dx}{dt} = \frac{\alpha_H(T_M - T_s)}{\rho_s\left[q_s + (T_M - T_s)c_{p(l)}\right]} \quad (51)$$

where α_H is the heat transfer coefficient; ρ_s is the scrap density, kg/m^3; T_s is the temperature of scrap, °C; and $C_{p(l)}$ is the liquid-specific heat capacity of scrap, kJ/(kg·°C).

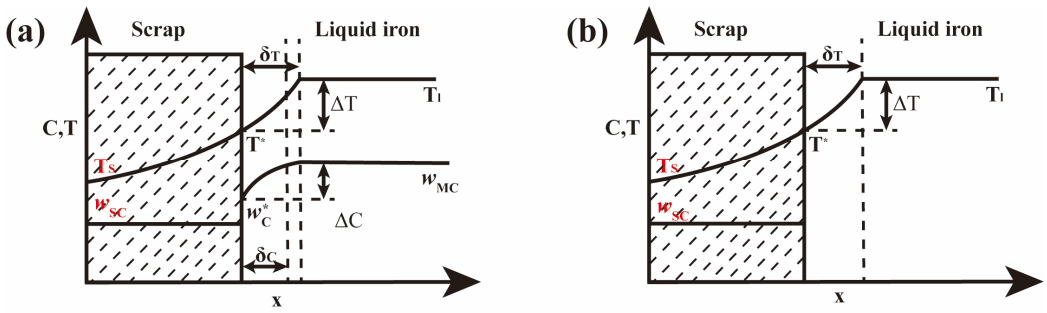

Figure 5. The temperature and concentration distributions during scrap melting. (**a**) mass transfer-controlled scrap melting; (**b**) heat transfer-controlled scrap melting.

When the liquidus temperature of scrap is higher than the bath temperature, the melting of scrap is related to the heat transfer rate and the mass transfer rate of carbon. The melting rate of scrap can be calculated according to the heat and mass transfer process using Equations (52) and (53).

$$V_{Scrap} = -\frac{dx}{dt} = \frac{\alpha(T_M - T^*)}{\rho_s\left[q_s + (T_M - T^*)c_{p(l)}\right]} \quad (52)$$

$$V_{Scrap} = -\frac{dx}{dt} = \frac{\beta\left(w_{MC} - w_C^*\right)\rho_l}{\left(w_{MC} - w_C^*\right)\rho_s} \quad (53)$$

where ρ_l is the melt density, kg/m^3; w_C^* is the carbon content at the interface between the scrap and the melt, wt%.; and T* is the temperature at the interface between the scrap and the melt, °C.

The amount of molten steel in the molten pool can be calculated using Equation (54).

$$W_{\text{Molten pool}} = W_{\text{Hot metal}} + W_{\text{MScrap}} - (\Delta W_{\text{HC}} + \Delta W_{\text{HSi}} + \Delta W_{\text{HMn}} + \Delta W_{\text{HP}} + \Delta W_{\text{HS}} + \Delta W_{\text{Fe}}) \quad (54)$$

2.5. Calculation of Heat Loss Coefficient

During the converter-smelting process, the high-temperature melt can continuously transfer heat to the furnace and the air; thus, a certain degree of heat loss inevitably occurs. The heat loss coefficient is usually set as a constant during the heat balance calculation of the converter. However, due to the different smelting times, hot metal temperatures, and other conditions, the heat loss coefficient differs.

Figure 6 shows the statistical results of the heat loss coefficients of the 130 t converter. As shown in Figure 6, the heat loss coefficient of the converter is distributed between 3 and 17%, among which 87.85% of the heat loss coefficients are between 6 and 11%, and 66.73% of the heat loss coefficients are between 7 and 10%. The heat loss coefficient difference between different heats is relatively large. Setting the heat loss coefficient simply as a fixed value is inappropriate.

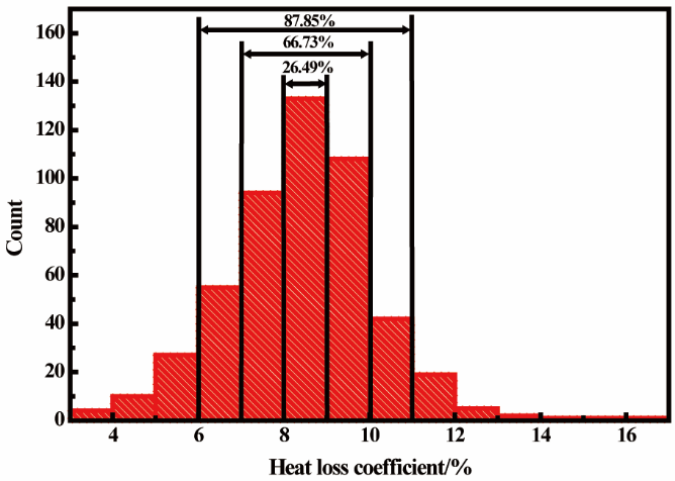

Figure 6. Frequency distribution histogram of heat loss coefficient of the 130 t converter.

In order to determine the heat loss coefficient of each hot metal more accurately, multiple linear regression was used to calculate the heat loss coefficient in this study. SPSS software (Version: IBM SPSS Statistic 25) was used to establish a multiple linear regression model for the heat loss coefficient of the converter. The input variables of the model included the weight of hot metal; the temperature of hot metal; the weight of scrap; the contents of C, Si, Mn, P, and S in hot metal; the temperature of molten steel; the content of C, Mn, P, and S in molten steel; the charging time; melting time; and the consumption of sintering, magnesium balls, lime, and lightly burned dolomite. The data items were filtered in the process of multiple linear regression, and the parameters with high correlation were selected for the construction of the model.

The heat production data of 1051 130 t converters were collected, where the heat production data of 851 were used for multiple linear regression analysis, and the data of 150 furnaces were used for model validation. The multiple linear regression equation for the heat loss coefficient of the converter can be expressed as follows:

$$\begin{aligned}\gamma_{\text{Loss}} = {} & 0.00004888 \times V_{O_2} - 0.004316 \times W_{\text{Scrap}} + 0.071662 \times w_{\text{HSi}} - 0.000007614 \times W_{\text{Lime}} + 0.000248 \times \\ & T_{\text{Hot metal}} - 0.001534 \times W_{\text{Hot metal}} - 0.000008984 \times W_{\text{LBD}} - 0.0000007909 \times W_{\text{Coolant}} + 0.008066 \times w_{\text{HMn}} + \\ & 0.063206 \times w_{\text{HP}} - 0.261918\end{aligned} \quad (55)$$

where W_{Coolant} is the weight of coolant, kg.

3. Model Validation and Discussion

3.1. Implementation of the Model Using Finite Difference Method

The numerical procedure uses the explicit finite difference method, which advances in time and solves for the results of the next time step using the parameters calculated in the previous time step. Parameters such as molten steel composition and temperature can be considered approximately constant at each different time step. The converter temperature prediction model is implemented in the C++ programming language. Figure 7 shows the flow chart of the calculation program for the complete mathematical model. After starting the calculation, the hot metal composition, temperature and addition, the scrap addition, as well as the charging process and the oxygen-blowing process are entered into the calculation program as initial parameters. The time step is set to 1 s. After the initiation of the calculation program, the scrap-melting rate, the lime-melting rate, and the oxidation process of C, Si, Mn, P, and Fe in the molten pool are calculated. At the same time, the thermal income, including the physical heat of the hot metal, the oxidation heat of each element in the melt pool, and the thermal expenditure (such as the physical heat of furnace gas, physical heat of soot, and physical heat of sputtered metal), are also calculated. In this study, it is assumed that the dust weight is 1.6% of the hot metal weight, and the sputtered metal weight is 1% of the hot metal weight. The physical heat of the soot and the physical heat of the sputtered metal are equally distributed throughout the blowing process.

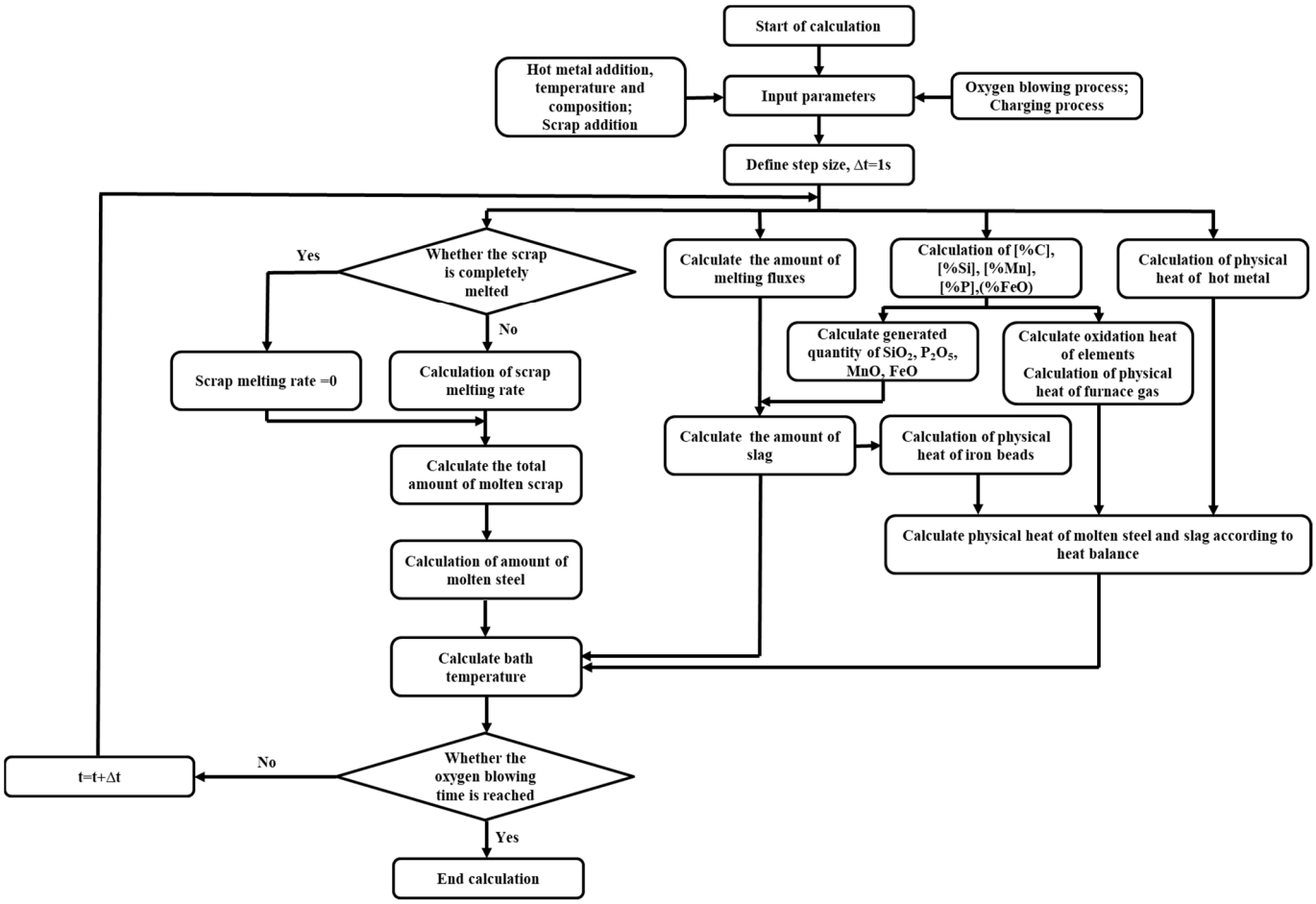

Figure 7. The flow chart of the calculation program for the complete mathematical model.

3.2. Composition and Temperature Verification in Converter-Blowing Process

In this paper, the actual production data of a 130t converter in China were collected in order to correct the model and adjust the model parameters. The raw material conditions of the 130t converter are listed in Table 1.

Table 1. Raw material conditions of the 130t converter.

	Amount/t	T/°C	C/%	Si/%	Mn/%	P/%	S/%
Hot metal	124.05	1301	4.12	0.30	0.28	0.107	0.0025
Scrap	23.4	25	--	--	--	--	--

The specific values of some parameters in the model are shown in Table 2.

Table 2. The values of some parameters in the model.

Model Parameter	Value	Unit	Model Parameter	Value	Unit
c_m^s	0.745	KJ/(kg·°C)	q_{Dust}	209.2	KJ/kg
c_m^l	0.8368	KJ/(kg·°C)	β	0.98	/
q_m	217.568	KJ/kg	α	5.68×10^{-6}	/
c_s^s	0.699	KJ/(kg·°C)	k_1	2.25×10^{-7}	/
c_s^l	0.8368	KJ/(kg·°C)	k_3	2.3845×10^{-4}	/
q_s	271.96	KJ/kg	k	2.4773×10^{-5}	m/s
c_{Slag}	1.247	KJ/(kg·°C)	α_H	39,000	W/(m^2·°C)
c_{Dus}	1.0	KJ/(kg·°C)	ρ_s	7200	Kg/m^3
c_{Gas}	1.136	KJ/(kg·°C)	$Cp_{(1)}$	0.8368	KJ/(kg·°C)
q_{Slag}	209.2	KJ/kg			

The 130 t converter-blowing process targeted in this study is basically fixed. Figure 8 shows the 130 t converter oxygen-blowing process. The 130 t converter adopts a low-oxygen lance position smelting mode. The opening oxygen lance position is 2.14 m, and the oxygen lance position is gradually reduced in the early blowing stage. The main blowing oxygen lance position is 1.6 m. At the final stage of smelting, the oxygen lance position is lowered again to achieve a uniform steel composition temperature. The oxygen-blowing flow rate in the early blowing stage rapidly increases from 28,000 Nm^3/h to 28,200 Nm^3/h for blowing. At the end of the blowing process, as the molten steel composition in the melt pool meets the requirements, the amount of oxygen blowing will be properly reduced to prevent oxygen waste.

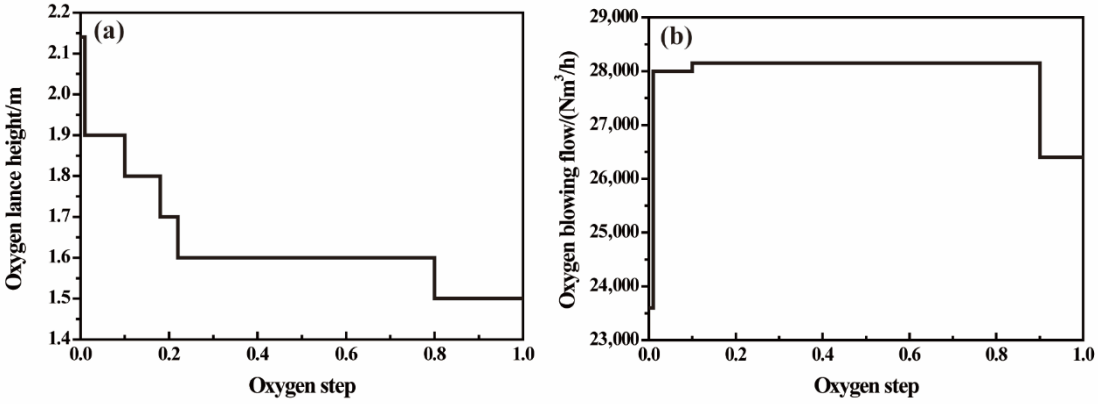

Figure 8. The oxygen-blowing process of the 130 t converter. (**a**) Oxygen lance position; (**b**) oxygen lance flow rate.

The flux-adding process of the 130 t converter is shown in Table 3. Lime, lightly burned dolomite, and magnesium balls were added in the first half of the blowing process. The lime was added in two batches. In the first batch, 73.5% of the total lime was added to the converter at 14% of the total oxygen-blowing volume; in the second batch, 26.5% of the total lime was added at 32.6% of the total oxygen-blowing volume. In summary, the flux-adding process is mainly concentrated in the early stage of converter blowing.

Table 3. Charging process of the 130 t converter.

Oxygen Step	Lime	Lightly Burned Dolomite	Magnesium Ball
0.009		1514	
0.014	2634		354
0.129			
0.326	949		

Figure 9 illustrates the simulated profiles of the carbon and phosphorus contents as a function of the blowing time. As shown in Figure 9a, the prediction result of the decarburization model is consistent with the universally recognized decarbonization law. The final predicted carbon content result is basically the same as the actual detected endpoint carbon content result. The difference between the endpoint carbon content calculated using the model and the actual carbon content of molten steel is 0.001%. Figure 9b illustrates the change in the phosphorus content in the molten pool with time. The phosphorus content rapidly decreases in the early stage, and the dephosphorization efficiency gradually retards in the middle and final stages. Due to the high iron oxide content in the steel slag during the smelting process, there is no rephosphorization phenomenon. The difference between the phosphorus content in molten steel calculated using the model and the actual endpoint phosphorus content is 0.0003%.

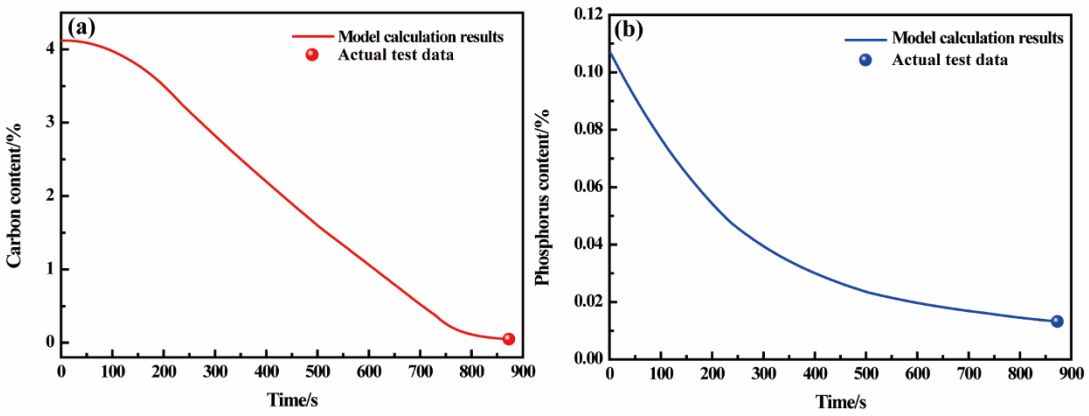

Figure 9. Model prediction of hot metal composition during the converter blowing: (**a**) carbon, (**b**) phosphorus.

Figure 10 illustrates the simulated profiles of the converter bath temperature as a function of the blowing time. At the beginning of blowing, no flux was added, and the melting speed of the scrap steel was relatively slow, so the temperature of the molten pool rapidly increased. As the added flux started to melt and the melting speed of the scrap steel accelerated, the heat income in the molten pool was used to melt the scrap steel and fluxes. At this stage, the temperature rose slowly. After the scrap was melted, the heat income in the molten pool was used to raise the temperature of the molten pool, and the rising speed of the temperature of the molten pool accelerated again. The predicted result of the model was in good agreement with the endpoint temperature detected by the sublance at the final blowing stage. The error between the endpoint molten steel temperature calculated using the model and the actual molten steel temperature was 3.2 °C.

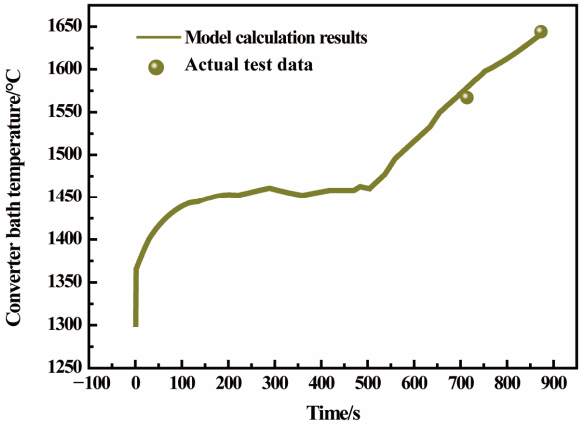

Figure 10. Calculated molten bath temperature using the model during the blowing process.

Figure 11 shows the weight change of the molten steel in the bath during converter blowing. The weight of molten steel in the molten pool continuously increased due to the continuous melting of scrap after the start of blowing. When the blowing process was conducted for 505 s, the weight of the steel reached the maximum, and the scrap was fully melted, as shown in Figure 12. After the scrap was fully melted, the weight of the molten steel began to decrease due to the oxidation reaction of elements in the molten pool. After the converter blowing, the molten steel weight calculated using the model was 136,192 kg, and the actual molten steel weight was 136,000 kg. The error is only 192 kg. The accurate prediction of the molten steel weight is beneficial to improving the accuracy of the model for predicting the terminal molten steel temperature.

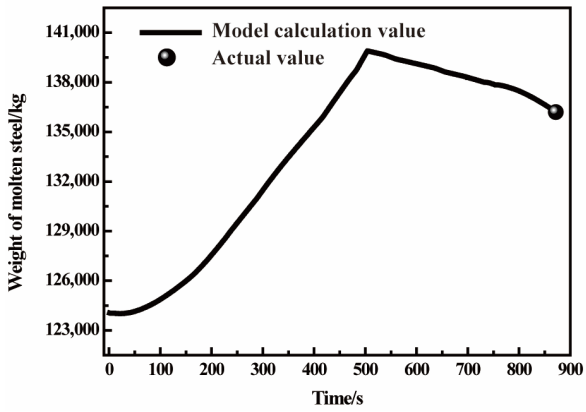

Figure 11. Weight of molten steel in the bath during converter blowing.

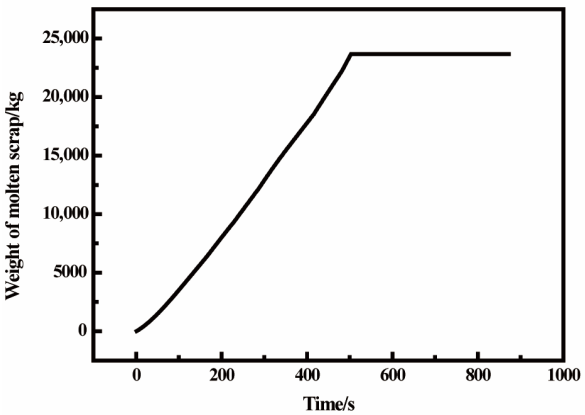

Figure 12. Weight of scrap melted during converter blowing.

3.3. Endpoint Temperature Hit Rate Verification

Figure 13 shows the validation results of the temperature model with a fixed heat loss coefficient. As shown in Figure 13a, a significant error was observed between the predicted values of the model and the actual values, indicating that the predicted value was inconsistent with the actual value. As shown in Figure 13b, the error was between −133 and 93 °C. When the error range is limited to ±20 °C, the model hit rate is only 51.3%. Moreover, when the error range is limited to ±15 °C, the model hit rate is 40.7%. During the smelting process of the converter, the high-temperature melt continuously transfers heat to the cooling system of the converter and air, resulting in heat loss. Due to different conditions, including the smelting time and molten iron temperature, the heat loss coefficient of each furnace differs. Therefore, the fixed heat loss coefficient cannot reflect the difference between iron temperatures, resulting in the poor accuracy of the converter endpoint molten steel temperature model.

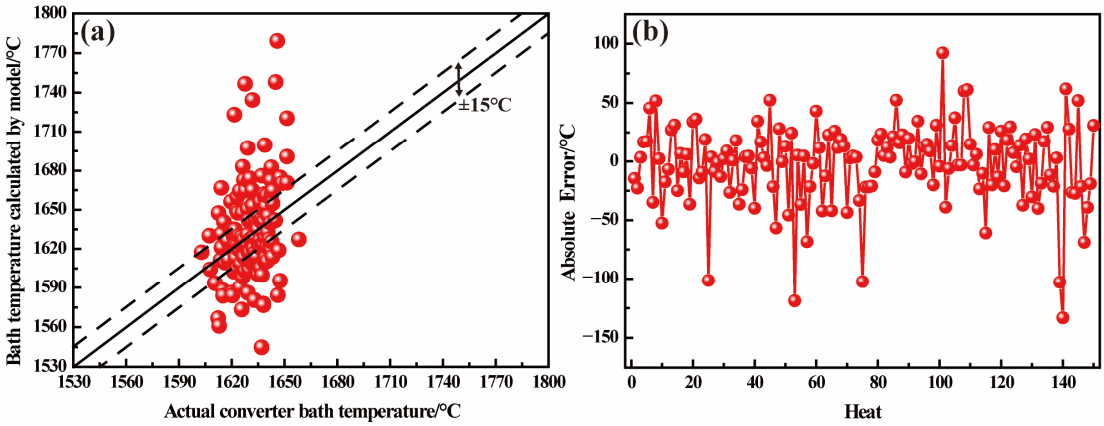

Figure 13. Comparison between operation data and predicted values using the temperature model with a fixed heat loss coefficient: (**a**) the comparison of endpoint molten steel temperature between the actual value and the predicted value; (**b**) the errors of the endpoint molten steel temperature.

Figure 14 shows the validation results of the temperature model with a heat loss coefficient obtained through regression. A certain improvement was observed in the consistency between the predicted values of the model and the actual values (Figure 14a). The difference between the model calculation results and the actual results of most iron temperatures was approximately 15 °C. Figure 14b shows the absolute errors of the temperature model with a heat loss coefficient obtained through regression. As shown in Figure 14b, the absolute error was between −26 and 24 °C. When the error range is limited to ±20 °C, the model hit rate reaches 96%. Moreover, when the error range is limited to ±15 °C, the model hit rate is 86.7%. This study establishes a multiple linear regression model for heat loss coefficients in order to obtain accurate heat loss coefficients. The heat loss coefficient becomes a parameter that varies with the change in data items. In the face of frequent changes in the furnace conditions, the heat loss coefficient determined based on regression models is more suitable for the current furnace conditions, and the accuracy of endpoint temperature prediction is greatly improved.

Figure 15 shows the comparison between the actual heat loss coefficient and calculation values of the multiple linear regression. The model used for calculating the heat loss coefficient established in this study has good calculation accuracy. The error between the calculated and actual heat loss coefficients is approximately 1.3%. In addition, the root mean squared error (RMSE) is 0.49%. The accurate calculation of the heat loss coefficient makes the accuracy of the temperature prediction model much better.

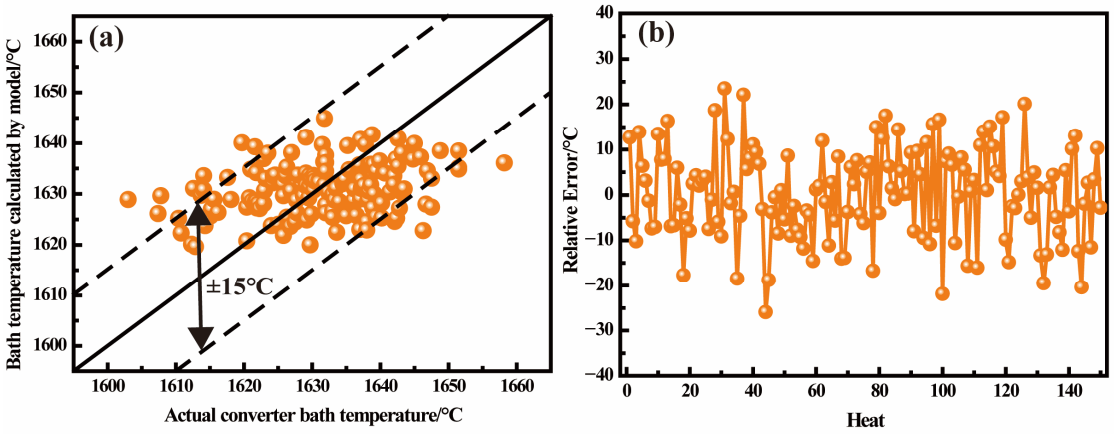

Figure 14. Comparison between operation data and predicted values using the temperature model with the heat loss coefficient obtained using regression: (**a**) the comparison between the actual endpoint temperature and the predicted value of the model; (**b**) the absolute errors of the model.

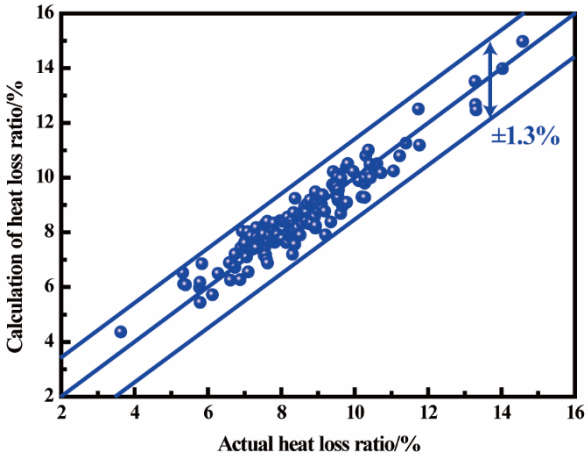

Figure 15. Comparison between the actual heat loss coefficient and calculation values of multiple linear regression.

3.4. The Effect of Scrap Weight on Temperature of Molten Pool

Scrap steel not only consumes a large part of the heat in the converter, but also is one of the main factors affecting the temperature curve of molten steel. Therefore, the influence of scrap quantity on the molten pool temperature is discussed in this study. Figure 16 shows the effect of scrap weight on the molten pool temperature. The less scrap is added, the shorter the time required for complete scrap melting in the early converting stage. When the amount of scrap is 18, 23, and 28 t, the times required for the complete melting of scrap are 459, 503, and 548 s, respectively. In the scrap-melting stage, the temperature of the molten pool increases as the scrap quantity decreases. This phenomenon occurs because, when the amount of scrap is small, the amount of scrap rapidly melted is relatively small, and more heat is used for the temperature rise of the molten pool. Therefore, reducing the amount of scrap can increase the bath temperature in the early and middle stages of converter blowing and shorten the melting time of scrap. Moreover, the endpoint temperature of molten steel will also rise when the amount of scrap is reduced. Without the addition of a heating agent, the endpoint temperature of molten steel can increase by about 50°C when the amount of scrap is reduced by 5 t.

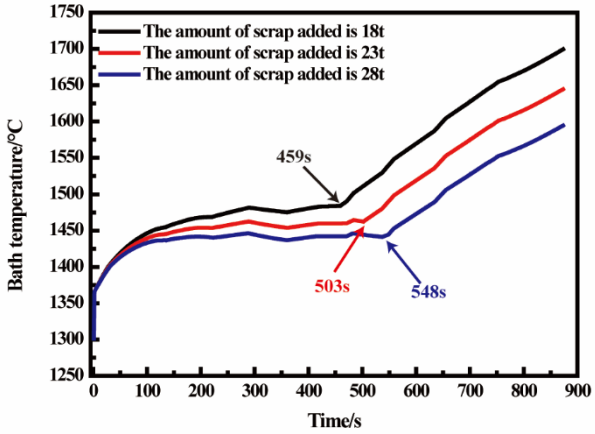

Figure 16. Effect of scrap weight on temperature of molten pool.

4. Conclusions

In this study, a model used for the prediction of the temperature of molten steel was developed based on the element reaction, slag-forming process, and scrap-melting process, and the accuracy of the model was effectively improved by obtaining the heat loss coefficient through a statistical method.

(1) Given the element reaction in the bath, slagging process, and scrap-melting process, the temperature change process of molten steel calculated using the model was relatively consistent with the actual smelting process.

(2) The accuracy of the model was greatly improved after the heat loss coefficient was calculated using the multiple linear regression method. When the error range was limited to ±20 °C, the model hit rate was 96%. In addition, when the error range was limited to ±15 °C, the model hit rate was 86.7%.

(3) Scrap steel influenced the temperature of molten steel in the converter. When less scrap was added, the faster the melting speed, the higher the steel temperature in the early and middle stages of the converter-blowing process, and the higher the temperature of the molten steel at the final stage.

Author Contributions: Conceptualization, F.G., D.W. and Y.B.; Methodology, F.G. and D.W.; Software, F.G. and D.W.; Validation, F.G. and X.L.; Formal Analysis, F.G. and L.X.; Investigation, F.G.; Resources, Y.B.; Writing—Original Draft Preparation, F.G.; Writing—Review and Editing, F.G., Y.B. and L.Z.; Supervision, L.Z.; Project Administration, Y.B.; Funding Acquisition, Y.B. All authors have read and agreed to the published version of the manuscript.

Funding: This research received no external funding.

Data Availability Statement: All the data are given in the manuscript.

Conflicts of Interest: The authors have declared no conflict of interest.

References

1. Ocheri, C.; Ajani, O.O.; Daniel, A.; Agbo, N. The steel industry: A stimulus to national development. *J. Powder Metall. Min.* **2017**, *6*, 2–5.
2. Mattom, J.; Herrick, P.; Agrawal, V.M. An Overview of Indian Steel Industry and Its Impact on Construction Sector. In *Recent Trends in Civil Engineering*; Springer: Singapore, 2021; pp. 197–206.
3. Kumar, S.; Kumar, V. Effective Project Management in Steel Industry. *Asian J. Manag.* **2017**, *8*, 1379–1386. [CrossRef]
4. Guo, Z.C.; Fu, Z.X. Current situation of energy consumption and measures taken for energy saving in the iron and steel industry in China. *Energy* **2010**, *35*, 4356–4360. [CrossRef]
5. Han, Y.; Zhang, C.J.; Wang, L.; Zhang, Y.-C. Industrial IoT for intelligent steelmaking with converter mouth flame spectrum information processed by deep learning. *IEEE Trans. Ind. Inform.* **2019**, *16*, 2640–2650. [CrossRef]
6. Wang, X.; Wang, H. Converter practice in China with respect to steelmaking and ferroalloys. *Miner. Process. Extr. Metall.* **2019**, *128*, 46–57. [CrossRef]

7. Han, B.; Wei, G.; Zhu, R.; Wu, W.; Jiang, J.J.; Feng, C.; Dong, J.F.; Hu, S.Y.; Liu, R.Z. Utilization of carbon dioxide injection in BOF–RH steelmaking process. *J. CO2 Util.* **2019**, *34*, 53–62. [CrossRef]
8. Zhang, J.; Wang, G. Energy saving technologies and productive efficiency in the Chinese iron and steel sector. *Energy* **2008**, *33*, 525–537. [CrossRef]
9. Zhang, Y.; Zhang, C.; Zeng, K.; Zhu, L.; Han, Y. Research on terminal control model of intelligent mining of flame spectral information of converter mouth in late smelting stage. *Ironmak. Steelmak.* **2021**, *48*, 677–684. [CrossRef]
10. Wu, L.; Yang, N.; You, X.; Xing, K.; Hu, Y. A temperature prediction model of converters based on gas analysis. *Procedia Earth Planet. Sci.* **2011**, *2*, 14–19. [CrossRef]
11. Liu, C.; Tang, L.; Liu, J. A stacked autoencoder with sparse Bayesian regression for end-point prediction problems in steelmaking process. *IEEE Trans. Autom. Sci. Eng.* **2019**, *17*, 550–561. [CrossRef]
12. Branca, T.A.; Fornai, B.; Colla, V.; Murri, M.M.; Streppa, E.; Schröder, A.J. The Challenge of Digitalization in the Steel Sector. *Metals* **2020**, *10*, 288. [CrossRef]
13. Ellis, J.L.; Jacobs, M.; Dijkstra, J.; van Laar, H.; Cant, J.P.; Tulpan, D.; Ferguson, N. Synergy between mechanistic modelling and data-driven models for modern animal production systems in the era of big data. *Animal* **2020**, *14*, s223–s237. [CrossRef] [PubMed]
14. He, F.; Zhang, L. Prediction model of end-point phosphorus content in BOF steelmaking process based on PCA and BP neural network. *J. Process Control* **2018**, *66*, 51–58. [CrossRef]
15. Zhou, K.-X.; Lin, W.-H.; Sun, J.-K.; Zhang, J.-S.; Zhang, D.-Z.; Feng, X.-M.; Liu, Q. Prediction model of end-point phosphorus content for BOF based on monotone-constrained BP neural network. *J. Iron Steel Res. Int.* **2022**, *29*, 751–760. [CrossRef]
16. Wang, Z.; Chang, J.; Ju, Q.-P.; Xie, F.-M.; Wang, B.; Li, H.-W.; Wang, B.; Lu, X.-C.; Fu, G.-Q.; Liu, Q. Prediction model of end-point manganese content for BOF steelmaking process. *ISIJ Int.* **2012**, *52*, 1585–1590. [CrossRef]
17. Wang, X.; Han, M.; Wang, J. Applying input variables selection technique on input weighted support vector machine modeling for BOF endpoint prediction. *Eng. Appl. Artif. Intell.* **2010**, *23*, 1012–1018. [CrossRef]
18. Han, Z.; Liu, Y.; Zhao, J.; Wang, W. Real time prediction for converter gas tank levels based on multi-output least square support vector regressor. *Control Eng. Pract.* **2012**, *20*, 1400–1409. [CrossRef]
19. Qi, L.; Liu, H.; Xiong, Q.; Chen, Z. Just-in-time-learning based prediction model of BOF endpoint carbon content and temperature via vMF mixture model and weighted extreme learning machine. *Comput. Chem. Eng.* **2021**, *154*, 107488. [CrossRef]
20. Li, W.; Wang, Q.M.; Wang, X.S.; Wang, H. Endpoint prediction of BOF steelmaking based on BP neural network combined with improved PSO. *Chem. Eng. Trans.* **2016**, *51*, 475–480.
21. Rao, S.K.; Imam, R.; Ramanathan, K.; Pushpavanam, S. Sensitivity analysis and kinetic parameter estimation in a three way catalytic converter. *Ind. Eng. Chem. Res.* **2009**, *48*, 3779–3790. [CrossRef]
22. Koltsakis, G.C.; Konstantinidis, P.A.; Stamatelos, A.M. Development and application range of mathematical models for 3-way catalytic converters. *Metals* **1997**, *12*, 161–191. [CrossRef]
23. Wang, D.; Gao, F.; Xing, L.; Chu, J.; Bao, Y. Continuous Prediction Model of Carbon Content in 120 t Converter Blowing Process. *Metals* **2022**, *12*, 151. [CrossRef]
24. Rout, B.K.; Brooks, G.; Rhamdhani, M.A.; Li, Z.; Schrama, F.N.H.; Sun, J. Dynamic model of basic oxygen steelmaking process based on multi-zone reaction kinetics: Model derivation and validation. *Metall. Mater. Trans. B* **2018**, *49*, 537–557. [CrossRef]
25. Kitamura, S. Dissolution behavior of lime into steelmaking slag. *ISIJ Int.* **2017**, *57*, 1670–1676. [CrossRef]
26. Zhang, M.; Li, J.; Xue, Z.; Zhu, R.; Mou, Q.; Zhu, H. Evolution of physicochemical properties of quick lime at converter-smelting temperature. *High Temp. Mater. Process.* **2021**, *40*, 32–39. [CrossRef]
27. Vieira, L.M.; de Oliveira, H.C.C.; Telles, V.B.; Junca, E.; Vieira, E.A.; de Oliveira, J.R. Influence of lime particle and slag properties on lime dissolution in BOF converter. *J. Mater. Res. Technol.* **2020**, *9*, 14878–14886. [CrossRef]
28. Deng, H.; Wang, N.; Chen, M.; Zhang, G. Dissolution behaviour of limestone in converter slag: Evolution of microstructure and reaction interface. *Ironmak. Steelmak.* **2020**, *47*, 417–423. [CrossRef]
29. Penz, F.M.; Schenk, J. A Review of Steel Scrap Melting in Molten Iron-Carbon Melts. *Steel Res. Int.* **2019**, *90*, 1900124. [CrossRef]
30. Li, J.; Provatas, N. Kinetics of scrap melting in liquid steel: Multipiece scrap melting. *Metall. Mater. Trans. B* **2008**, *39*, 268–279. [CrossRef]
31. Kruskopf, A. A model for scrap melting in steel converter. *Metall. Mater. Trans. B* **2015**, *46*, 1195–1206. [CrossRef]
32. Wei, G.; Zhu, R.; Tang, T.; Dong, K. Study on the melting characteristics of steel scrap in molten steel. *Ironmak. Steelmak.* **2019**, *46*, 609–617. [CrossRef]
33. Kruskopf, A.; Holappa, L. Scrap melting model for steel converter founded on interfacial solid/liquid phenomena. *Metall. Res. Technol.* **2018**, *115*, 201. [CrossRef]
34. Deng, S.; Xu, A. Steel scrap melting model for a dephosphorisation basic oxygen furnace. *J. Iron Steel Res. Int.* **2020**, *27*, 972–980. [CrossRef]